NeuroImage: Clinical 29 (2021) 102518

Contents lists available at ScienceDirect

NeuroImage: Clinical

journal homepage: www.elsevier.com/locate/ynicl

Atlas-independent, N-of-1 tissue activation modeling to map optimal regions of subthalamic deep brain stimulation for Parkinson disease

Karlo A. Malaga [a,1], Joseph T. Costello [b], Kelvin L. Chou [c,d], Parag G. Patil [a,c,d,*]

[a] Department of Biomedical Engineering, University of Michigan, Ann Arbor, MI, USA
[b] Department of Electrical Engineering, University of Michigan, Ann Arbor, MI, USA
[c] Department of Neurology, University of Michigan, Ann Arbor, MI, USA
[d] Department of Neurosurgery, University of Michigan, Ann Arbor, MI, USA

ARTICLE INFO

Keywords:
Deep brain stimulation
Parkinson disease
Subthalamic nucleus
Diffusion tensor imaging
Electric field modeling
Tissue activation volume

ABSTRACT

Background: Motor outcomes after subthalamic deep brain stimulation (STN DBS) for Parkinson disease (PD) vary considerably among patients and strongly depend on stimulation location. The objective of this retrospective study was to map the regions of optimal STN DBS for PD using an atlas-independent, fully individualized (N-of-1) tissue activation modeling approach and to assess the relationship between patient-level therapeutic volumes of tissue activation (VTAs) and motor improvement.

Methods: The stimulation-induced electric field for 40 PD patients treated with bilateral STN DBS was modeled using finite element analysis. Neurostimulation models were generated for each patient, incorporating their individual STN anatomy, DBS lead position and orientation, anisotropic tissue conductivity, and clinical stimulation settings. A voxel-based analysis of the VTAs was then used to map the optimal location of stimulation. The amount of stimulation in specific regions relative to the STN was measured and compared between STNs with more and less optimal stimulation, as determined by their motor improvement scores and VTA. The relationship between VTA location and motor outcome was then assessed using correlation analysis. Patient variability in terms of STN anatomy, active contact position, and VTA location were also evaluated. Results from the N-of-1 model were compared to those from a simplified VTA model.

Results: Tissue activation modeling mapped the optimal location of stimulation to regions medial, posterior, and dorsal to the STN centroid. These regions extended beyond the STN boundary towards the caudal zona incerta (cZI). The location of the VTA and active contact position differed significantly between STNs with more and less optimal stimulation in the dorsal-ventral and anterior-posterior directions. Therapeutic stimulation spread noticeably more in the dorsal and posterior directions, providing additional evidence for cZI as an important DBS target. There were significant linear relationships between the amount of dorsal and posterior stimulation, as measured by the VTA, and motor improvement. These relationships were more robust than those between active contact position and motor improvement. There was high variability in STN anatomy, active contact position, and VTA location among patients. Spherical VTA modeling was unable to reproduce these results and tended to overestimate the size of the VTA.

Conclusion: Accurate characterization of the spread of stimulation is needed to optimize STN DBS for PD. High variability in neuroanatomy, stimulation location, and motor improvement among patients highlights the need for individualized modeling techniques. The atlas-independent, N-of-1 tissue activation modeling approach presented in this study can be used to develop and evaluate stimulation strategies to improve clinical outcomes on an individual basis.

1. Introduction

Deep brain stimulation (DBS) of the subthalamic nucleus (STN) is an established surgical treatment for the motor symptoms of medically intractable Parkinson disease (PD) (Benabid et al., 2009; Okun, 2012). The treatment involves implanting electrodes in the subthalamic region

* Corresponding author at: 1500 E. Medical Center Dr. SPC 5338, Ann Arbor, MI 48109-5338, USA.
E-mail address: pgpatil@med.umich.edu (P.G. Patil).
[1] Present address: Department of Biomedical Engineering, Bucknell University, Lewisburg, PA, USA.

https://doi.org/10.1016/j.nicl.2020.102518
Received 16 July 2020; Received in revised form 25 November 2020; Accepted 27 November 2020
Available online 3 December 2020
2213-1582/© 2020 The Author(s). Published by Elsevier Inc. This is an open access article under the CC BY-NC-ND license (http://creativecommons.org/licenses/by-nc-nd/4.0/).

of the brain and then applying electrical stimulation to this region (Collins et al., 2010). Despite the proven clinical effectiveness of DBS, motor improvement can vary considerably from one patient to another (Deuschl et al., 2006; Kleiner-Fisman et al., 2006; Okun et al., 2005). The underlying mechanism by which DBS provides its therapeutic effect is still uncertain (Ashkan et al., 2017; Deniau et al., 2010; Florence et al., 2016; Johnson et al., 2008; McIntyre and Hahn, 2010; McIntyre et al., 2004c; Montgomery and Gale, 2008; Vitek, 2002). However, it is widely accepted that DBS outcomes depend strongly on where stimulation is applied (Conrad et al., 2018; Maks et al., 2009; McIntyre et al., 2004b). Differences in the location of stimulation relative to the STN may, in part, explain the variability in motor improvement across patients.

The location of stimulation is typically defined by measuring the position of the active electrode contact relative to an anatomical reference point (Caire et al., 2013). The limitation of this approach is that it does not consider the full spatial extent of stimulation. This could explain why there are conflicting findings regarding the relationship between active contact position and motor improvement (Bot et al., 2018; Koivu et al., 2018; McClelland et al., 2005; Nestor et al., 2014; Paek et al., 2008; Verhagen et al., 2019; Wodarg et al., 2012). When stimulation is applied by the active contact, an electric field is induced in the brain tissue that spreads outward in all directions. Due to the difficulty in measuring the stimulation field experimentally, modeling techniques have been used to characterize the spatial distribution of the DBS-induced electric field (Butson, 2012). From this, the theoretical amount of tissue directly affected by stimulation, termed the volume of tissue activation (VTA), can be calculated (Astrom et al., 2009; Butson et al., 2007). The VTA is a stimulation-dependent metric that can be used to predict clinical outcomes (Avecillas-Chasin et al., 2019; Butson et al., 2006), optimize stimulation settings (Frankemolle et al., 2010; McIntyre et al., 2009), explore alternative surgical targets (Miocinovic et al., 2006; Zitella et al., 2013), and evaluate novel electrode designs (Butson and McIntyre, 2006; Howell et al., 2015; van Dijk et al., 2015). The utility of tissue activation modeling hinges on its ability to make accurate and clinically meaningful predictions. Substantial efforts have gone towards validating VTA predictions with experimental data (Miocinovic et al., 2009; Zitella et al., 2015).

Tissue activation modeling has become increasingly complex over time. Neurostimulation models can now incorporate detailed anatomical information, heterogeneous and anisotropic tissue properties, explicit representation of the DBS lead and electrode-tissue interface, clinically determined stimulation settings, and biophysical neuron models (Chaturvedi et al., 2010; Gunalan et al., 2017, 2018; Howell and McIntyre, 2016). The primary motivation for each of these advancements has been a more accurate and patient-specific characterization of the spatial extent of stimulation. Previous studies have shown tissue anisotropy to be one of the most relevant factors impacting model prediction accuracy (Astrom et al., 2012; Cardona et al., 2016; Howell and McIntyre, 2017; Ineichen et al., 2018; Schmidt and van Rienen, 2012). However, tissue properties are typically derived from a brain atlas instead of individual patient data when creating tailored neurostimulation models (Butson et al., 2011). Since some brain atlases are based on a single subject, there is a limitation in how representative an atlas is to a patient population, especially one that is in a Parkinsonian state (Dickie et al., 2017; Nowacki et al., 2018).

The objective of this study was to map, for the first time, the regions of optimal STN DBS in an atlas-independent, fully individualized (N-of-1) manner. The relationship between the location of anatomically and electrically accurate VTAs and motor improvement was then assessed. Such an approach can be extended to the study of fiber tracts in the subthalamic region that are hypothesized to ameliorate the symptoms of PD, specifically in terms of their location relative to the VTA.

The stimulation-induced electric field for 40 PD patients treated with bilateral STN DBS was modeled using finite element analysis. Neurostimulation models were generated for each patient, incorporating their individual STN anatomy, DBS lead position and orientation, anisotropic tissue conductivity, and clinical stimulation settings. A voxel-based analysis of the VTAs was then used to map the optimal location of stimulation. The amount of stimulation in specific regions relative to the STN was measured and compared between STNs with more and less optimal stimulation, as determined by their motor improvement scores and VTA. The relationship between VTA location and motor outcome was then assessed using correlation analysis. Patient variability in terms of STN anatomy, active contact position, and VTA location, as well as a simplified VTA modeling approach, were also evaluated, highlighting the need for atlas-independent, N-of-1 modeling techniques.

2. Methods

2.1. Patient selection

In this study, patients were drawn from a prospectively acquired clinical database of individuals who received bilateral STN DBS for PD at the University of Michigan. Selection criteria included an established diagnosis of idiopathic PD and the availability of pre-operative magnetic resonance (MR) and diffusion tensor (DT) imaging, post-operative computed tomography (CT) imaging, and clinical follow-up assessments at least six months after surgery (Chou and Taylor, 2013). Patients with structural brain abnormalities on MR imaging or comorbid neuropsychiatric disorders, such as dementia and depression, were excluded. Forty patients were selected, resulting in 80 brain hemispheres for analysis. Of the 80 hemispheres, eight were later excluded due to having non-monopolar stimulation (three left and five right). Informed consent was obtained from all patients in accordance with the policies of the Medical Institutional Review Board (IRB) at the University of Michigan.

2.2. Deep brain stimulation surgery and programming

All patients underwent awake, frame-based DBS surgery. Final DBS lead placement was guided by MR imaging, stereotactic navigation, and microelectrode recording. The surgical procedure used has been previously reported (Conrad et al., 2018; Houshmand et al., 2014; Patil et al., 2012). By six months after surgery, all patients had stable DBS programming parameters and satisfactory clinical outcomes.

2.3. Image acquisition and processing

Pre-operative 3-T MR images were acquired for each patient at their baseline evaluation. Post-operative CT images were acquired two to four weeks after surgery to allow pneumocephalus to resolve, thereby minimizing its effect on electrode position (Bentley et al., 2017). The MR and CT imaging protocols used have been previously reported (Patil et al., 2012). Briefly, MR imaging was performed using a Philips Achieva 3T scanner with the following settings: slice orientation = coronal, field of view = FH 200, voxel size = FH 0.69, RL 0.69, and AP 1.25, slice thickness = 1.25, gap = 0, SENSE factor = 1.8, number of slices = 40, fold-over direction = R/L, scan mode = 3-D, technique = IR, fast imaging mode = TSE, TSE factor = 58, echo time = 200 ms, repetition time = 6000 ms, NSA = 1, and scan duration = 7:18. CT imaging was performed using a GE HD750 64-slice scanner with the following settings: scan type = axial, HiRes mode = on, gantry rotation time/length = 1.0 s full, detector coverage = 20 mm, slice thickness = 0.625 mm, number of images/rotation = 32i, interval = 20 mm, KVP/mA = 140/450, ASIR = SS40%, recon mode = full, DFOV = 27–29 cm, SFOV = head, and algorithm = HD standard. Pre-operative 3-T DT images were also acquired at baseline using a single-shot echo-planar imaging sequence combined with dS SENSE, a parallel imaging scheme used to decrease image distortion (Jaermann et al., 2004). Diffusion weighting was encoded along 15 independent orientations with a b-value of 800 mm^2/s. Diffusion tensor imaging parameters included a $1 \times 1 \times 2$ mm voxel size, 224×224 mm field-of-view, and reduction factor of 2.

Magnetic resonance and DT images were resampled using linear and cubic spline interpolation, respectively, to match the resolution of the CT images (Houshmand, 2015). Magnetic resonance images were transformed to Talairach space, where the anterior and posterior commissures lie on a straight horizontal line (Talairach and Tournoux, 1988). The midcommissural point (MCP) was defined as the origin, with positive x, y, and z corresponding to the right hemisphere, anterior direction, and dorsal direction, respectively. Computed tomography and DT images were oriented to Talairach space via co-registration to the MR images using a normalized mutual information algorithm and manual refinement. All image processing was performed by the same individual to minimize co-registration variability using Analyze (12.0, AnalyzeDirect, Inc., Overland Park, KS, USA).

2.4. Clinical evaluation

Part III of the Movement Disorders Society revision of the Unified Parkinson Disease Rating Scale (MDS-UPDRS III) was used to evaluate the severity of individual motor symptoms (Chou and Taylor, 2013). Post-operative scores without medication for rigidity, bradykinesia, and tremor were used instead of baseline scores to isolate the stimulation-specific effects of DBS from those associated with surgery or disease progression. Scores were measured either 6 (24/40 patients), 12 (12/40 patients), or 24 (4/40 patients) months after surgery. Rigidity scores came from item 3.3 (max 8), bradykinesia scores from items 3.4–3.8 (max 20), and tremor scores from items 3.15–3.17 (max 16). Scores were lateralized to their appropriate hemisphere. Axial symptoms, such as speech and posture, were excluded from analysis. Motor improvement was defined as

$$improvement[\%] = \frac{score_{OFFmed/OFFstim} - score_{OFFmed/ONstim}}{score_{OFFmed/OFFstim}} \times 100$$

2.5. Atlas-independent, N-of-1 tissue activation modeling

Multi-step, electric field modeling techniques using atlas-based anatomical nuclei and tissue properties have been previously developed (Astrom et al., 2009; Butson et al., 2007). In this study, an atlas-independent, N-of-1 tissue activation modeling approach building from these previous works was designed to increase the accuracy of VTA modeling on an individual-patient basis (Fig. 1). The N-of-1 modeling approach is described below (Section 2.5.1-4).

2.5.1. Subthalamic nucleus segmentation

Three-dimensional (3D) anatomical models of the STNs were created for each patient from their MR imaging (72 STNs total). Subthalamic nuclei were manually traced from coronal slices using Analyze. Visualization of the STN was optimized by maximizing the contrast between it and the substantia nigra pars reticulata (Conrad et al., 2018; Houshmand et al., 2014; Patil et al., 2012). All STNs were traced by the same individual and validated by the neurosurgeon who performed the DBS surgeries to minimize segmentation variability. Traces of the STN were then exported to MATLAB (R2018b, The MathWorks, Inc., Natick, MA, USA) for analysis.

2.5.2. Electrode contact localization

All patients were implanted with quadripolar DBS leads (model 3389, Medtronic, Inc., Minneapolis, MN, USA). Electrode contacts were localized in the brain of each patient from their CT imaging (288 contacts total and 72 active contacts). Contact coordinates were measured

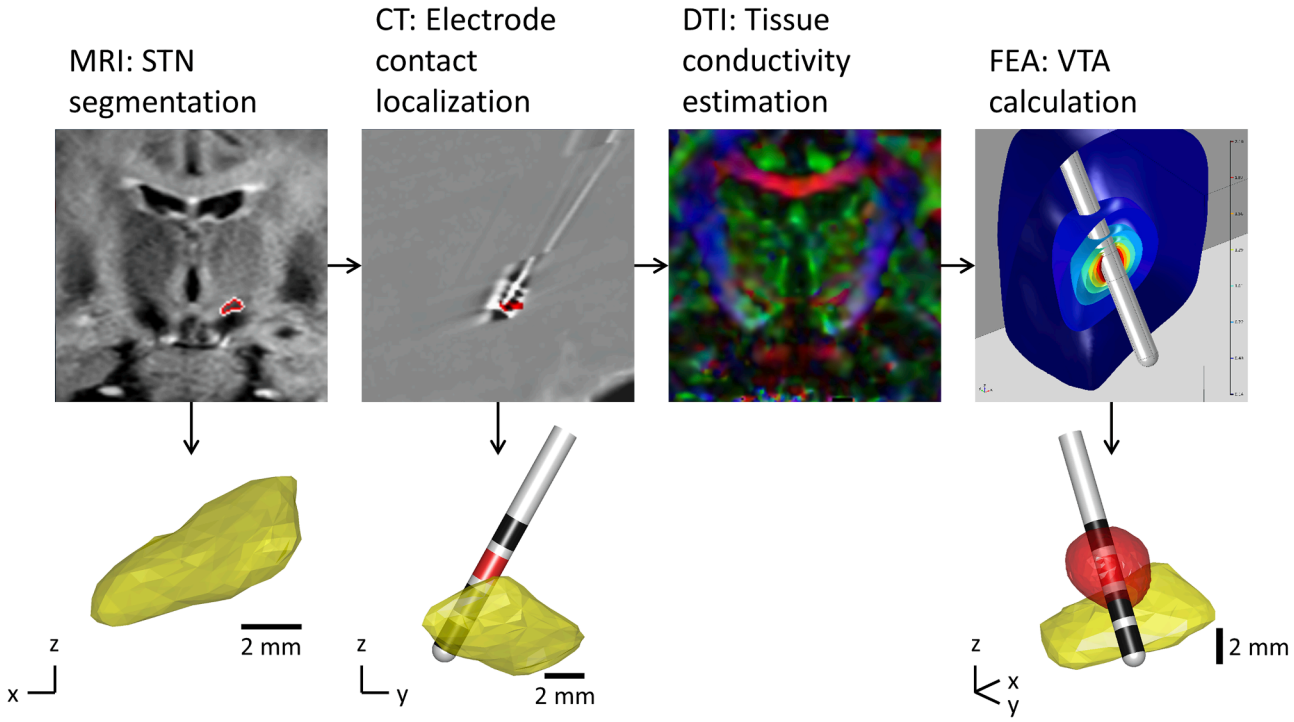

Fig. 1. Atlas-independent, N-of-1 tissue activation modeling approach. *Subthalamic nucleus segmentation.* Top: coronal MR image for one patient showing the left (outlined in red) and right STN. Bottom: left STN in MATLAB after STN segmentation. *Electrode contact localization.* Top: sagittal CT image showing the electrode contacts (black) of the left DBS lead and the STN mask (red). Bottom: left STN and DBS lead in MATLAB after electrode contact localization. *Diffusion tensor imaging-based anisotropic tissue conductivity estimation.* Coronal DT image showing the calculated eigenvector color map. Red, green, and blue correspond to the x, y, and z direction, respectively. *Finite element analysis.* Top: deep brain stimulation-induced potential distribution around the active contact in COMSOL. Colors correspond to different isolevels in volts. Bottom: left STN (yellow), DBS lead (red: active contact, dark gray: inactive contacts), and VTA (red; defined by the thresholded electric field norm) in MATLAB after finite element analysis. Positive x, y, and z correspond to the right hemisphere, anterior direction, and dorsal direction, respectively. (For interpretation of the references to color in this figure legend, the reader is referred to the web version of this article.)

from 3D reconstructions using Analyze. Visualization of the electrode contacts was optimized via CT windowing (Conrad et al., 2018; Patil et al., 2012). All contact positions were measured by the same individual and validated by the neurosurgeon who performed the DBS surgeries to minimize localization variability. Contact coordinates were then exported to MATLAB for analysis.

2.5.3. Diffusion tensor imaging-based anisotropic tissue conductivity estimation

The anisotropic electrical conductivity of the brain tissue was estimated for each patient from their individual DT imaging (40 tensor fields total). Diffusion eigenvalue and eigenvector maps were calculated using the Diffusion Tensor Imaging add-on in Analyze and then exported to MATLAB, where they were converted to 3D diffusion tensors on a per-voxel basis using matrix diagonalization (Houshmand, 2015). Diffusion tensor fields were converted to conductivity tensor fields (Tuch et al., 2001) and then exported to COMSOL Multiphysics (5.2, COMSOL, Inc., Burlington, MA, USA) for finite element analysis.

2.5.4. Finite element analysis

Three-dimensional finite element models (FEMs) incorporating individual brain anatomy, DBS lead position and orientation, anisotropic tissue conductivity, and clinical stimulation settings were created for each hemisphere of each patient (72 FEMs total) to calculate the spatial distribution of the DBS-induced electric field and estimate the therapeutic VTA (Astrom et al., 2009; Butson et al., 2007). The bulk brain tissue was modeled as a block surrounding the DBS lead (Medtronic 3389). The block of tissue had a width, length, and depth equal to that of the patient's brain, as measured on MR imaging, and the cylindrical lead had a contact length of 1.5 mm, contact spacing of 0.5 mm, and electrode diameter of 1.27 mm. The DBS lead was translated and rotated such that the electrode contacts best matched the measured contact coordinates. The bulk tissue domain was assigned the DT imaging-based anisotropic electrical conductivity by linearly interpolating the conductivity tensors onto the mesh. The remaining domains, contact and insulation, were assigned isotropic conductivities of $1.42e^{7}$ S/m and $1e^{-13}$ S/m, respectively (Kent and Grill, 2014). Boundary conditions were defined for the electrode contacts and bulk tissue. An electric potential equal to the patient's therapeutic stimulation amplitude was applied to the surface of their therapeutic electrode contact (active contact) and ground was applied to the bottom surface of the bulk tissue (Pelot et al., 2018). The remaining electrode contacts were disabled. Finite element models were then meshed, with finer meshing applied at and around the DBS lead. After testing for model convergence by modifying the mesh density, simulations were run to solve for the electric potential throughout the brain using the Poisson equation. All FEMs were electrostatic because the impedance of gray matter has been shown to be frequency-independent at stimulation frequencies relevant to clinical DBS (approximately 130 Hz) (Logothetis et al., 2007). The VTA was defined by the electric field norm, thresholded at stimulation-specific activation levels derived from biophysical neuron models (Astrom et al., 2015). Simulations and VTA predictions were performed using COMSOL. Tissue activation volumes were then exported to MATLAB, where their location relative to the STN was characterized for analysis.

2.6. Volume of tissue activation mapping

N-of-1 VTAs were placed into a common coordinate space (single hemisphere) via Procrustes superimposition. Briefly, each individual STN was flipped (to the right hemisphere if a left STN), translated, scaled, and rotated so that its centroid position, size, and major axis orientation matched that of the median STN (based on volume). The STN transformations were then applied to each associated VTA. The number of VTAs at each position (voxel) was calculated to identify the region of greatest VTA overlap. A clinical score reflecting the motor outcome of each patient (percent improvement) was assigned to the voxels comprising each VTA (Akram et al., 2017; Butson et al., 2011; Haegelen et al., 2018). The mean score was then calculated at each voxel to identify the optimal location of stimulation. Tissue activation volumes were mapped for improvement in rigidity, bradykinesia, and tremor. If patients did not exhibit a particular motor symptom, then their VTAs were excluded from the symptom-specific analysis.

2.7. Optimality of stimulation

Although some patients had similar motor outcomes, the size and shape of their N-of-1 VTAs often varied. Assuming an optimal location of stimulation exists, it was reasoned that patients with active contacts near said location would require less stimulation (and in turn have smaller VTAs) to gain therapeutic benefit from DBS (Conrad et al., 2018). A measure of the optimality (or efficiency) of stimulation was defined to differentiate patients with similar levels of motor improvement. This measure was the ratio of improvement and the VTA (%/mm^3). Patients with greater improvement and smaller VTAs were considered to have closer to optimal stimulation.

2.8. Statistical analysis

Paired, two-sided Wilcoxon signed rank tests were used to determine if post-operative assessments with DBS ON differed significantly from those with DBS OFF. For VTA mapping, a bootstrap analysis was performed in which the clinical scores were randomly assigned to each VTA (and its associated voxels) prior to averaging to distinguish statistically significant voxel-score pairs. This process was repeated 1000 times to create a null distribution of mean scores at each voxel. A voxel-score pair was determined significant if the actual mean score at that voxel was above the 95th percentile of the distribution. Two-sided Wilcoxon rank sum tests (equivalent to Mann-Whitney U-tests) were used to determine if measures of stimulation location for STNs with more optimal stimulation differed significantly from those for STNs with less optimal stimulation. Subthalamic nuclei were ranked according to their optimality of stimulation. The top and bottom 25% of STNs were then placed into the more and less optimal stimulation groups, respectively. The strength of the relationship between stimulation location and the optimality of stimulation was also assessed using Pearson linear correlation coefficients. All statistical analysis was performed using MATLAB. Significance was determined at a p-value of less than 0.05.

3. Results

3.1. Patient demographics, motor outcomes, and stimulation settings

Demographics for the entire patient cohort are provided in Table 1. Lateralized, post-operative rigidity, bradykinesia, and tremor scores from the MDS-UPDRS III improved significantly with DBS ON; and pre-operative LEDD decreased significantly with DBS ($p < 0.001$, Wilcoxon signed rank test). The rigidity, bradykinesia, and tremor scores improved by 1.2 points (56.2%), 3.0 points (36.9%), and 2.3 points (65.8%), respectively, on average (Table 2). LEDD decreased by 790.6 mg/d (55.4%) on average (Table 1). At each patient's post-operative assessment, the stimulation amplitude, frequency, and pulse width of the clinically active contact were recorded along with the associated impedance (Table 3).

3.2. Patient variability in STN anatomy and stimulation location

High variability in STN anatomy (location and size) and stimulation location (active contact position and VTA location) was observed across patients. The location of the STN was characterized by its centroid position relative to the MCP; and STN size was characterized by its width, length, depth, and volume. The STN centroid was located 11.13 ± 1.39

Table 1
Patient demographics and post-operative change in LEDD with DBS.

	n	Mean	Standard deviation	Minimum	Maximum
Age at baseline [yr]	40	63.1	6.7	52.7	74.7
Age at diagnosis [yr]	40	52.9	8.6	33	69
Disease duration at baseline [yr]	40	10.3	5.2	2	22.8
Time to follow-up [mo]	40	9.6	5.6	6	24
LEDD (pre-operative) [mg/d]	40	1370.5	777.6	0	3342
LEDD (post-operative) [mg/d]	40	579.9	459.3	0	1746
LEDD reduction [%]	36	55.4	33.4	−50	100

n: 40 patients total (28 male and 12 female; 36 with medication and 4 without medication); LEDD: L-DOPA equivalent daily dose.

Table 2
Post-operative change in lateralized MDS-UPDRS III scores with DBS.

	n	Mean	Standard deviation	Minimum	Maximum
Rigidity score (OFF med/OFF stim)	72	2.4	1.9	0	8
Rigidity score (OFF med/ON stim)	72	1.2	1.7	0	8
Rigidity improvement [%]	58 *	56.2	43.8	−50	100
Bradykinesia score (OFF med/OFF stim)	72	9.2	4.0	1	17
Bradykinesia score (OFF med/ON stim)	72	6.2	4.2	0	17
Bradykinesia improvement [%]	72	36.9	41.3	−166.7	100
Tremor score (OFF med/OFF stim)	72	3.2	4.0	0	15
Tremor score (OFF med/ON stim)	72	0.9	1.7	0	9
Tremor improvement [%]	41 *	65.8	41.4	−50	100

* When calculating improvement, hemispheres with an OFF med/OFF stim score of zero (0) were excluded.
n: 72 brain hemispheres total (37 left and 35 right; 58 with rigidity, 72 with bradykinesia, and 41 with tremor).

Table 3
Clinical DBS settings and electrode impedance.

	n	Mean	Standard deviation	Minimum	Maximum
Stimulation amplitude [V]	72	2.7	0.6	1.5	4.2
Stimulation frequency [Hz]	72	141.3	22.6	125	185
Stimulation pulse width [μs]	72	60.4	3.5	60	90
Electrode impedance [Ω]	71 *	1225.8	279.4	441	1902

* Impedance data unavailable for one hemisphere.
n: 72 brain hemispheres total (37 left and 35 right).

mm lateral (mean ± standard deviation), 0.92 ± 2.59 mm posterior, and 3.24 ± 1.22 mm ventral to the MCP. The width, length, depth, and volume of the STN were 7.91 ± 1.67 mm, 8.56 ± 1.45 mm, 5.19 ± 1.12 mm, and 80.9 ± 31.3 mm^3, respectively.

The location of each active contact was characterized by its position relative to the STN centroid (Conrad et al., 2018) (Fig. 2). Active contacts were located 0.21 ± 1.35 mm medial, 0.63 ± 1.93 mm posterior, and 0.79 ± 1.99 mm dorsal to the STN centroid. Plotting all 72 active contacts relative to the median STN showed that there was no obvious clustering in a particular region and that contacts were quite evenly distributed around the STN centroid in all directions.

The location of the VTA was measured in the native space of each patient and characterized by its percentage lateral, posterior, and dorsal to the STN centroid (lateral, posterior, and dorsal stimulation, respectively) (Fig. 3) as well as its percentage outside of the STN. Overall, 46.3 ± 28.1% of the VTA was lateral, 60.9 ± 33.1% was posterior, and 59.2 ± 33.0% was dorsal to the STN centroid. On average, over three-quarters of the VTA was outside of the STN (77.7 ± 16.3%). Tissue activation volumes were quite evenly distributed around the STN centroid in the lateral-medial direction. However, VTAs spread noticeably more posterior and dorsal than anterior and ventral due to local tissue anisotropy. This contrasts with active contact position, which was more evenly distributed. In all but two cases, over half of the VTA spread beyond the STN boundary.

3.3. Therapeutic VTA overlap

The region of greatest VTA overlap is shown in Fig. 4. This represents the overall stimulation region for the entire patient cohort following clinical DBS programming and assessment. The centroid of this region was located 0.20 mm medial and 0.80 mm posterior to the STN centroid (−0.20, −0.80, 0). In contrast, the optimal location of stimulation was mapped to regions medial, posterior, and dorsal to the STN centroid (Fig. 5). These regions extended beyond the STN boundary. The optimal location of stimulation generally remained in the same region regardless of the individual motor symptom. Optimal stimulation for rigidity encompassed a broad region dorsomedial to the STN. For bradykinesia, optimal stimulation was well-defined by VTA mapping and encompassed a focused region posterior to the STN centroid. Optimal stimulation for tremor was the broadest, encompassing a region almost entirely dorsal to the STN. Combining symptoms by summing their individual scores (overall improvement) yielded a VTA map that closely resembled that for bradykinesia. For rigidity, bradykinesia, tremor, and overall improvement, 58/72, 72/72, 41/72, and 72/72 N-of-1 VTAs, respectively, were analyzed.

3.4. Difference in stimulation location between more and less optimal stimulation

Subthalamic nuclei were ranked by their optimality of stimulation (ratio of motor improvement and the VTA) to determine if those with more and less optimal stimulation differed in terms of VTA location and active contact position. The top and bottom 25% of STNs were then placed into the more and less optimal stimulation groups, respectively. For bradykinesia, STNs in the more optimal stimulation group had significantly more dorsal stimulation and significantly more dorsal active contacts (relative to the STN centroid) than those in the less optimal stimulation group ($p < 0.05$, Mann-Whitney U-test). For rigidity, STNs in the more optimal stimulation group had significantly more posterior stimulation and significantly more posterior active contacts than those in the less optimal stimulation group ($p < 0.05$, Mann-Whitney U-test). For tremor, there were no significant differences between STNs in the more and less optimal stimulation groups in terms of VTA location and active contact position. These findings were consistent with the VTA mapping results (Fig. 5).

3.5. Relationship between stimulation location and motor improvement

Correlation analysis was also performed using all 72 STNs to assess the relationship between stimulation location and the optimality of stimulation. For rigidity, there were statistically significant linear relationships between the amount of posterior and dorsal stimulation (as measured by the VTA) and the optimality of stimulation (posterior: $r = 0.26$, $p = 0.046$, 95% CI = [0.01, 0.47]; dorsal: $r = 0.27$, $p = 0.04$, 95% CI = [−0.02, 0.49]). For bradykinesia, there was a significant

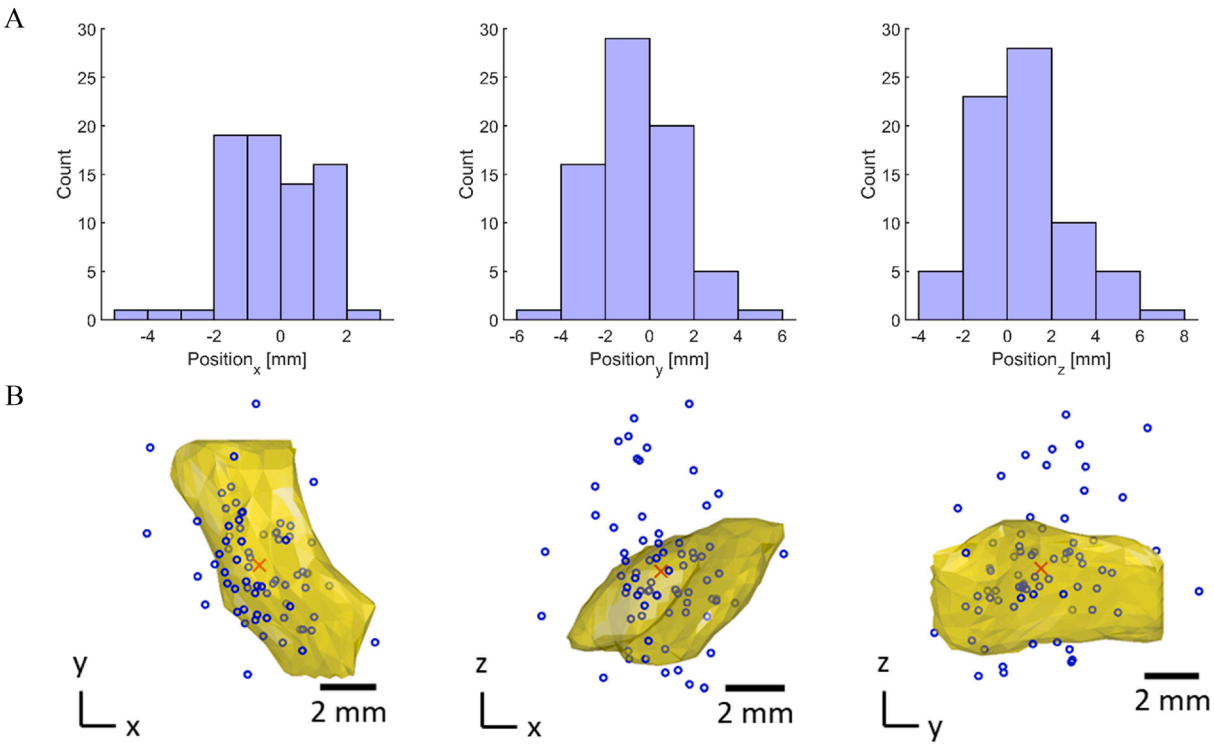

Fig. 2. Variability in active contact position relative to the STN centroid across patients. A. Histograms of active contact position in the lateral-medial, anterior-posterior, and dorsal–ventral directions. B. Scatter plots of active contact position for 72 implants (open, blue circles). The mean active contact position is shown as a red x and the median STN (based on volume) is shown in yellow. Contact positions from A were transformed to a common coordinate space (right hemisphere) based on the median STN. Axial, coronal, and sagittal views are shown. Positive x, y, and z correspond to the lateral, anterior, and dorsal direction, respectively. (For interpretation of the references to color in this figure legend, the reader is referred to the web version of this article.)

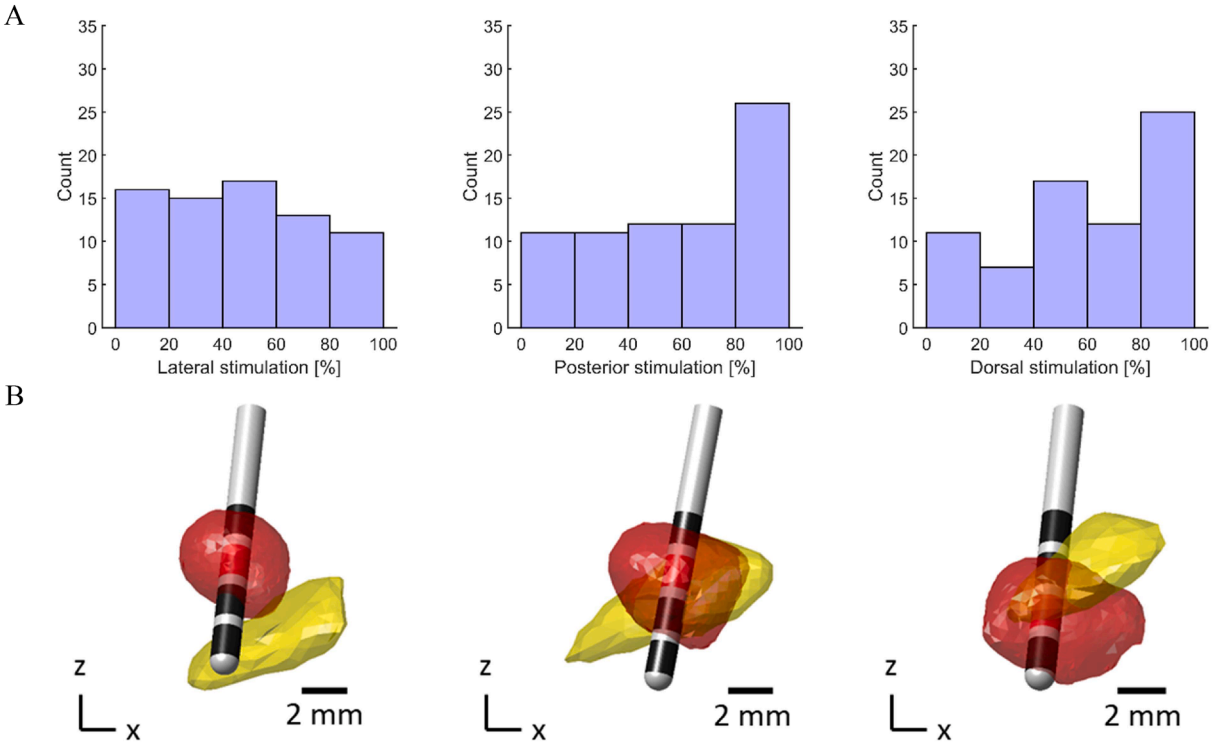

Fig. 3. Variability in VTA location relative to the STN centroid across patients. A. Histograms of VTA location in the lateral-medial, anterior-posterior, and dorsal–ventral directions. B. Three-dimensional exemplar models of the individual STN, DBS lead, and VTA for three patients using N-of-1 modeling. Note the differences in STN and VTA shape between patients. The STN is shown in yellow, active contact and VTA are shown in red, and inactive contacts are shown in dark gray. Coronal views are shown. Positive x and z correspond to the lateral and dorsal direction, respectively. (For interpretation of the references to color in this figure legend, the reader is referred to the web version of this article.)

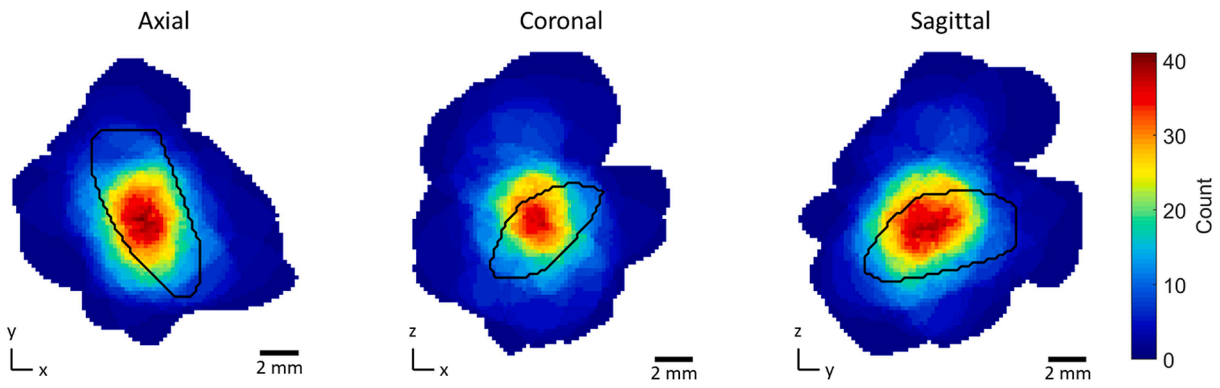

Fig. 4. Therapeutic VTA overlap. Map of the number of overlapping VTAs (72 VTAs total). Slices are at the STN centroid (origin). The median STN (based on volume) is shown as a black outline. Positive x, y, and z correspond to the lateral, anterior, and dorsal direction, respectively.

relationship between active contact position in the lateral-medial direction and the optimality of stimulation ($r = 0.28$, $p = 0.02$, 95% CI = [0.08, 0.46]). These findings were also consistent with the VTA mapping results (Fig. 5). For tremor, there was no statistically significant correlation between stimulation location and the optimality of stimulation. Compared to active contact position, VTA location generally had more robust relationships with motor improvement.

4. Discussion

Despite the proven clinical effectiveness of STN DBS, motor improvement can vary considerably from one patient to another. A possible explanation for this variability is differences in the precise location where stimulation is applied in the subthalamic region. Previous studies have highlighted the need for a more detailed identification of stimulation location relative to DBS targets, one that goes beyond simple active contact position (Caire et al., 2013; Nestor et al., 2014). In this study, an atlas-independent, fully individualized (N-of-1) tissue activation modeling approach was used to characterize the spatial extent of stimulation, termed the VTA, in 40 patients with PD who received bilateral STN DBS. Individual MR, CT, and DT imaging data were used to build each N-of-1 neurostimulation model, and individual clinical scores from the MDS-UPDRS III were assigned to the VTA predictions to assess the effectiveness of each stimulation zone. To the best of our knowledge, this study is the first to use a fully individualized VTA modeling approach to identify the optimal location of STN DBS for PD at this large a patient scale.

4.1. Patient variability in STN anatomy and stimulation location

High variability in STN anatomy and stimulation location (active contact position and VTA location) was observed across patients. Measurements for this analysis were taken in the native space of each patient. The anatomy of the STN was characterized by its location (centroid position relative to the MCP) and size (width, length, depth, and volume). The degree of neuroanatomical variability was similar to that reported in previous studies (Daniluk et al., 2010; Duchin et al., 2018; Massey et al., 2012; Patel et al., 2008; Richter et al., 2004; Xiao et al., 2014). To control for this variability, the STN centroid was chosen over the typically used MCP as the anatomical reference point when measuring active contact position and VTA location. A previous study has proposed alternative reference points for a similar reason (Bot et al., 2018). Despite using a more individualized reference point, active contacts were quite evenly distributed around the STN centroid in all directions (Fig. 2), making it difficult to determine an optimal location of stimulation based on active contact position alone. In contrast, therapeutic VTAs spread noticeably more into the posterior and dorsal halves of the STN (Fig. 3). Interestingly, the location of therapeutic stimulation varied considerably across patients. This finding highlights the need for individualized modeling techniques when characterizing stimulation location to optimize DBS for patients (Cubo et al., 2015).

4.2. Optimal location of stimulation

Overall, mapping the N-of-1 VTAs to a common coordinate space revealed the optimal location of stimulation to be in regions medial, posterior, and dorsal to the STN centroid. This finding is consistent with previous studies attempting to identify the optimal stimulation site for STN DBS (Akram et al., 2017; Butson et al., 2011; Conrad et al., 2018; Haegelen et al., 2018; Herzog et al., 2004; Maks et al., 2009; Pollo et al., 2007; Voges et al., 2002a; Yokoyama et al., 2006). The optimal location of stimulation extended outside the STN border. In contrast, the mean active contact was contained within the dorsal half of the STN. Therapeutic stimulation consistently spread beyond the STN, as confirmed by calculating the percentage of the VTA external to the STN. In 70/72 cases, over half of the total VTA lay outside the STN. These findings suggest that the optimal location of stimulation is dorsomedial to the STN, near the posterior half of the nucleus. This location did not vary markedly when motor symptoms were analyzed individually, suggesting that optimal stimulation sites for rigidity, bradykinesia, and tremor may overlap. The optimal location of stimulation was broad for rigidity and well-defined for bradykinesia. This finding is consistent with a previous modeling study (Butson et al., 2011).

The optimal stimulation site for STN DBS is still under debate (Plaha et al., 2006; Welter et al., 2014). Dorsolateral STN has been reported as the most effective site for stimulation (Guo et al., 2013; Richardson et al., 2009). However, the region dorsomedial to STN has also been reported as an effective stimulation site (Lanotte et al., 2002; Voges et al., 2002b). Electrophysiological studies have identified dorsal STN as an optimal site for stimulation based on it exhibiting high beta and high-frequency oscillation (HFO) activity. These signals have been investigated as possible biomarkers for optimizing DBS because of their correlation with motor improvement. In the dorsal STN region, high-frequency oscillation activity was found to be located slightly more superior than beta activity (van Wijk et al., 2017), which was found to be more widely distributed in the STN (Telkes et al., 2018). Furthermore, stronger HFO activity was found to be specific to patients with tremor-predominant PD (Telkes et al., 2018), which suggests one way that electrophysiological recordings could be incorporated into the N-of-1 VTA modeling approach to further optimize DBS targeting at the individual level (e.g., incorporating HFO power into the optimality measure). Although optimal stimulation sites exhibited high beta activity that was localized in the dorsal STN region (Lu et al., 2020b), it was found that these sites did not co-localize in the posterior-lateral STN region, but did in the posterior-medial STN region (Lu et al., 2020a). More specifically, maximal beta power co-localized with active contacts

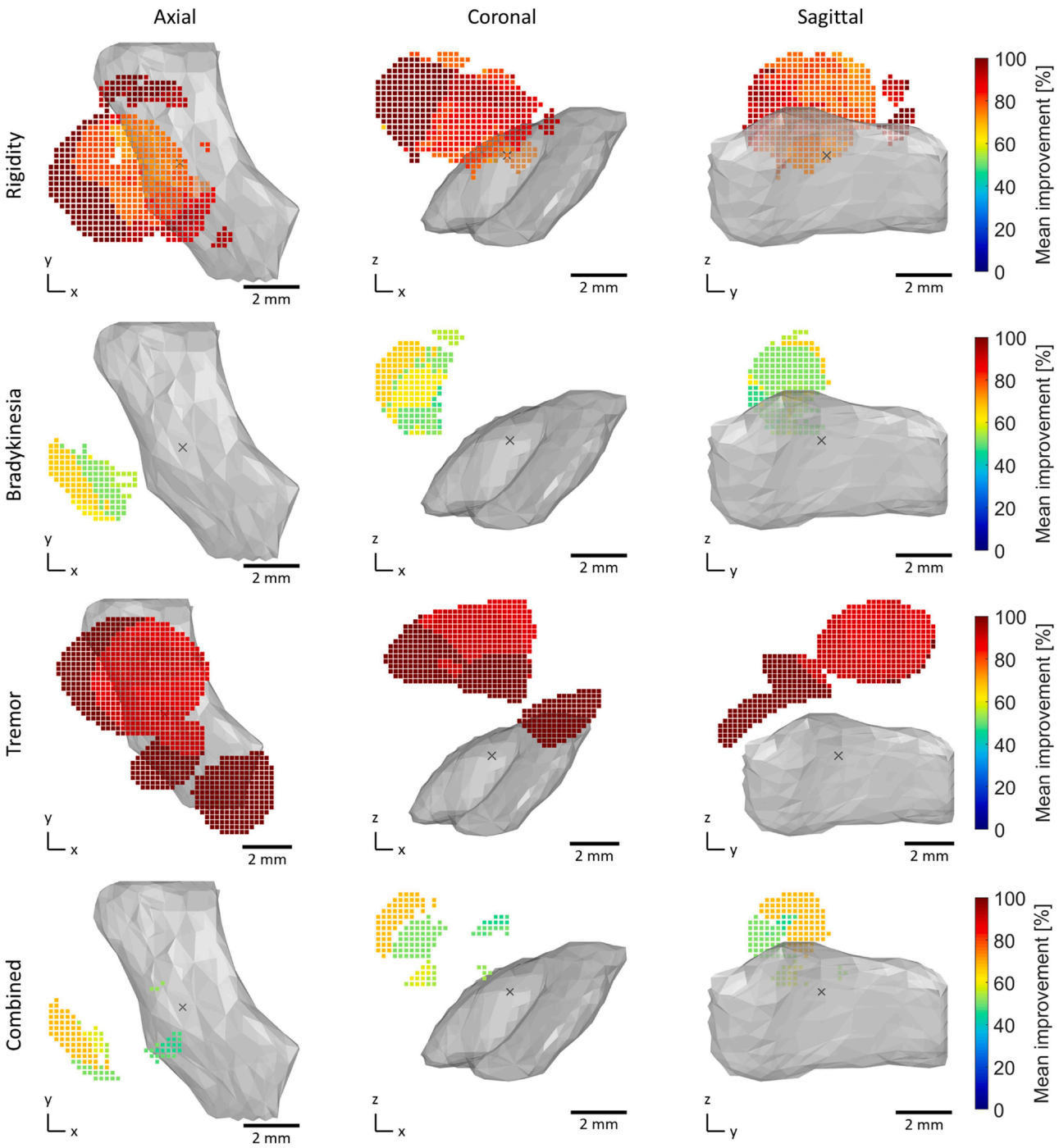

Fig. 5. Volume of tissue activation mapping of motor improvement for individual and combined symptoms. Three-dimensional maps of mean improvement at statistically significant voxels (determined via bootstrap analysis on the optimality measures) for rigidity (58/72 VTAs), bradykinesia (72/72 VTAs), tremor (41/72 VTAs), and combined symptoms (sum of individual symptom scores) (72/72 VTAs). The mean active contact position is shown as a black x and the median STN (based on volume) is shown as a gray surface. Positive x, y, and z correspond to the lateral, anterior, and dorsal direction, respectively.

at the dorsal border of the STN along trajectories passing posterior-medial to the STN midpoint. Alternative surgical targets have also been explored to better tailor treatment to the individual needs of PD patients (Anderson et al., 2017). These targets include the globus pallidus internus, ventral intermediate nucleus of the thalamus, and caudal zona incerta (cZI). The cZI, in particular, has recently been suggested as an overall superior target (Blomstedt et al., 2012; Plaha et al., 2006). The optimal location of stimulation identified in this study includes regions where the cZI is located in addition to the motor subregion of the STN (Alkemade, 2013) and the pallidothalamic and cerebellorubrothalamic fiber tracts. However, these specific structures were not explicitly modeled. It is also important to emphasize that this hotspot is a generalization. At the individual level, the therapeutic VTAs of multiple patients were found to deviate from the average optimal location of stimulation (Fig. 3).

4.3. *Difference in stimulation location between more and less optimal stimulation*

To validate the optimal location of stimulation identified from VTA

mapping, stimulation location was compared between STNs with more and less optimal stimulation. The optimality (or efficiency) of stimulation measure was defined as the ratio of motor improvement and the VTA, such that STNs with greater improvement and smaller VTAs were considered to have more optimal stimulation. The logic behind this measure was that patients with active contacts closer to some presumed optimal stimulation site would require less stimulation (and in turn have smaller VTAs) to gain therapeutic benefit from DBS (Conrad et al., 2018). Unlike for VTA mapping, measurements for this analysis were taken in the native space of each patient. Subthalamic nuclei were ranked according to their optimality of stimulation, and then separated into top and bottom quartiles. Once STNs were grouped, differences in VTA location and active contact position between the two groups were assessed. For bradykinesia, STNs with more optimal stimulation had significantly more dorsal stimulation and significantly more dorsal active contacts (relative to the STN centroid) than those with less optimal stimulation ($p < 0.05$). For rigidity, STNs with more optimal stimulation had significantly more posterior stimulation and significantly more posterior active contacts than those with less optimal stimulation ($p < 0.05$). These findings suggest that the optimal location of stimulation lies dorsal and posterior to the STN centroid, which is consistent with the VTA mapping results (Fig. 5). There was no significant difference in stimulation location found between the two groups for tremor. This was likely due to the lower number of tremor VTAs available and the fact that tremor was completely alleviated by DBS for most patients regardless of the size of their VTA.

4.4. Relationship between stimulation location and motor improvement

There is conflicting evidence in the literature regarding the relationship between coordinate-based electrode location and DBS motor outcome. Several studies have reported that electrode location can predict motor improvement (Bot et al., 2018; Verhagen et al., 2019), while others have reported that there is no significant correlation between the two variables (Koivu et al., 2018; McClelland et al., 2005; Nestor et al., 2014; Paek et al., 2008; Wodarg et al., 2012). Using individual STNs manually segmented from patient MR imaging (not an atlas STN warped to each patient), the position of the active contact relative to the STN centroid was measured in each implanted hemisphere. The STN centroid was chosen over the typically used MCP as the anatomical reference point to control for neuroanatomical variability across patients (Bot et al., 2018; Conrad et al., 2018). A correlation analysis was then performed between active contact position and the optimality of stimulation. Bradykinesia was the only motor symptom with a significant relationship between the two variables ($p < 0.05$), where more lateral electrode contacts were correlated with more optimal stimulation.

A key limitation of using active contact position to identify where stimulation is located is that it does not consider the full spatial extent of stimulation, which varies based on the DBS settings and electrical properties of the brain. Consequently, the correlation analysis was repeated using VTA location instead of active contact position. For rigidity, there were significant relationships between the amount of posterior and dorsal stimulation and the optimality of stimulation ($p < 0.05$). There was no statistically significant relationship between stimulation location and the optimality of stimulation for tremor, likely due to the reasons mentioned in the section above. Again, these findings are consistent with the VTA mapping results (Fig. 5). Additionally, there was no significant correlation between the amount of STN stimulation (VTA inside the STN) or the amount of external stimulation (proxy for ZI stimulation) and the optimality of stimulation, suggesting that the optimal location of stimulation may lie between the two structures (Falconer et al., 2018) or include both of them. Overall, VTA location had more robust relationships with motor improvement and showed greater predictive capability than active contact position. Combining these two measures of stimulation location may improve the reliability of models attempting to predict DBS clinical outcomes (Nestor et al., 2014). However, the lack of a strong relationship between therapeutic stimulation location and motor improvement supports the notion that there likely may not be a single hotspot that is optimal for all patients.

4.5. Limitations and alternative modeling approaches

In this study, neurostimulation models were tailored to each patient by incorporating their individual STN anatomy, DBS lead position and orientation, anisotropic tissue conductivity, and clinical stimulation settings to characterize the most accurate representation of their therapeutic stimulation field. Despite this, there are several limitations that should be considered when interpreting the results. First, the DBS outcomes evaluated only included rigidity, bradykinesia, and tremor, the primary motor symptoms of PD. Side effects and non-motor outcomes were not included in the overall analysis due to the unavailability of lateralized clinical scores. However, these outcomes can be readily incorporated into the N-of-1 modeling framework reported here, and future studies are planned to do so.

Second, only therapeutic electrode contacts and VTAs based on the clinically optimized stimulation settings of each patient were evaluated (one active contact and VTA per hemisphere per patient). The remaining three electrode contacts were not included in the overall analysis. This limited the spatial coverage of stimulation in the subthalamic region. However, given that the therapeutic contacts were quite evenly distributed around the STN centroid in all directions (Fig. 2), sufficient VTA coverage was still attained. Since a specific aim of this study was to determine the variability of therapeutic stimulation across patients, it made sense to focus on the clinically optimized stimulation settings of each patient, as determined through DBS programming and assessment. Stimulation settings (and VTAs) associated with side effects or other DBS outcomes can be analyzed in a similar manner, which planned future studies shall do.

Third, since multiple imaging modalities were required to create each neurostimulation model, image co-registration is a possible source of error. Image co-registration was performed using commercial software for visualizing and analyzing medical imaging (Analyze) to minimize error between pre- and post-operative imaging data. A normalized mutual information algorithm was used to precisely align the CT and DT imaging of each patient with their MR imaging (Studholme et al., 1998), and all co-registrations were done and evaluated by the same individual. If deemed necessary by visual inspection, manual refinements were made to ensure an accurate co-registration. Fourth, the brain was assumed to be purely resistive and linear with regard to DBS (Bedard et al., 2004). Consequently, all FEMs built were electrostatic. Previous experimental studies have shown that the impedance of gray matter is frequency-independent at stimulation frequencies relevant to clinical DBS (Logothetis et al., 2007). Furthermore, previous modeling studies have shown that it is reasonable to ignore the capacitive properties of brain tissue (Grant and Lowery, 2010; Howell and McIntyre, 2016; Schmidt et al., 2013). Regardless, possible limitations with electrostatic solutions, such as when adaptive, burst, or kilohertz frequency stimulation paradigms are used, can be addressed by frequency-dependent models combined with impedance spectroscopy measurements that account for the resistive and capacitive properties of the tissue (Butson and McIntyre, 2005; Lempka and McIntyre, 2013). Fifth, FEM solutions were not coupled to biophysical neuron models to determine the VTA. Instead, the VTA was defined by activation field strength thresholds of the electric field (Astrom et al., 2015). These thresholds were derived for clinically relevant stimulation amplitudes and pulse widths using axon cable models. An exponential was fit to the activation field thresholds corresponding to an axon diameter of 2.5 μm and a stimulation pulse width of 60 μs to calculate the individual thresholds for each patient based on their therapeutic stimulation amplitude. Astrom et al. showed that the VTA can be approximated by a constant electric field threshold without the need to couple axon models to the FEM solution (Astrom

et al., 2015). This greatly reduces computation time, which is highly favorable since an intended application of this work is to run simulations to test and optimize stimulation settings for patients in a clinical setting. However, it is important to note that their analyses were performed using isotropic tissue conductivities. Lastly, tractography was not incorporated into the individualized modeling framework. Several studies have used tractography to aid in identifying optimal stimulation sites for treating PD with DBS (Akram et al., 2017; Avecillas-Chasin et al., 2019; Garcia-Gomar et al., 2017; Gunalan et al., 2017; O'Halloran and Chartrain, 2016). This is of interest because DBS is hypothesized to elicit its therapeutic effect through a combination of axonal activation and cellular inhibition (McIntyre et al., 2004a; McIntyre and Hahn, 2010). The DT imaging data used to estimate the anisotropic tissue conductivity for each patient can also be used to perform tractography. Doing so would allow direct comparison of gray and white matter stimulation, such as the hyperdirect pathway and internal capsule, and their effects on DBS outcomes (Akram et al., 2017; Chen et al., 2018; Gunalan et al., 2017). However, the accuracy of the tractography results would be limited by the voxel resolution of the DT imaging (Rodrigues et al., 2018).

Regarding clinical application of the individualized modeling framework reported here, alternative methods of modeling the VTA are available (Cubo et al., 2017; Madler and Coenen, 2012). One such approach uses a sphere centered at the active contact to estimate the VTA, where the radius of the sphere is a function of the stimulation amplitude and electrode impedance (Madler and Coenen, 2012). To assess the validity of this approximation, the analysis was repeated using spherical VTAs in place of fully individualized VTAs. Spherical VTA models were unable to reproduce the results presented in this study and tended to overestimate the size of the VTA (Supplementary Fig. 1). Previous studies have described VTA overestimation as a possible limitation of simplified modeling approaches (Butson and McIntyre, 2005; Chaturvedi et al., 2006). While simplified VTA modeling approaches can be useful in identifying general regions where stimulation would be therapeutic, they are limited in their ability to optimize stimulation at the individual patient level because they typically do not consider tissue anisotropy, one of the most relevant factors impacting VTA prediction accuracy. Driving-force algorithms offer an alternative modeling strategy to quantify the cellular response to the DBS-induced electric field in a clinical setting, one that is both highly detailed and computationally feasible (Gunalan et al., 2018; Howell et al., 2019).

5. Conclusion

Accurate characterization of the spread of stimulation in the brain is important for optimizing STN DBS for PD. High variability in neuroanatomy, stimulation location, and motor improvement across patients highlights the need for individualized modeling techniques. Using an atlas-independent, N-of-1 tissue activation modeling approach, this study mapped the optimal location of stimulation to regions dorsomedial to the STN, near the posterior half of the nucleus. This location did not vary markedly when motor symptoms were analyzed individually, suggesting that optimal stimulation sites for rigidity, bradykinesia, and tremor may overlap. Therapeutic stimulation spread noticeably more in the dorsal and posterior directions, providing additional evidence for cZI as an important DBS target. The N-of-1 modeling approach presented in this study can be used to develop and evaluate stimulation strategies to improve clinical outcome on an individual basis. Furthermore, these methods can be used to investigate the non-motor and side effects associated with STN DBS and be extended to other conditions treated with DBS, such as essential tremor and depression, to identify other optimal stimulation sites.

Declaration of Competing Interest

K.L.C. has served on an advisory board for Boston Scientific.

Acknowledgements

The authors would like to thank the patients involved in this study for their voluntary participation, Kelly J. Lupo for image processing and electrode contact localization, and Charles W Lu for insightful discussions of preliminary results. This material is based upon work supported by the National Science Foundation Graduate Research Fellowship (K.A. M.), Ford Foundation Predoctoral Fellowship (K.A.M.), and University of Michigan Rackham Merit Fellowship (K.A.M.), and the A. Alfred Taubman Medical Research Institute.

Appendix A. Supplementary data

Supplementary data to this article can be found online at https://doi.org/10.1016/j.nicl.2020.102518.

References

Akram, H., Sotiropoulos, S.N., Jbabdi, S., Georgiev, D., Mahlknecht, P., Hyam, J., Foltynie, T., Limousin, P., De Vita, E., Jahanshahi, M., Hariz, M., Ashburner, J., Behrens, T., Zrinzo, L., 2017. Subthalamic deep brain stimulation sweet spots and hyperdirect cortical connectivity in Parkinson's disease. NeuroImage 158, 332–345.
Alkemade, A., 2013. Subdivisions and anatomical boundaries of the subthalamic nucleus. J. Neurosci. 33, 9233–9234.
Anderson, D., Beecher, G., Ba, F., 2017. Deep brain stimulation in Parkinson's disease: new and emerging targets for refractory motor and nonmotor symptoms. Parkinsons Dis. 2017, 5124328.
Ashkan, K., Rogers, P., Bergman, H., Ughratdar, I., 2017. Insights into the mechanisms of deep brain stimulation. Nat. Rev. Neurol. 13, 548–554.
Astrom, M., Zrinzo, L.U., Tisch, S., Tripoliti, E., Hariz, M.I., Wardell, K., 2009. Method for patient-specific finite element modeling and simulation of deep brain stimulation. Med. Biol. Eng. Comput. 47, 21–28.
Astrom, M., Lemaire, J.J., Wardell, K., 2012. Influence of heterogeneous and anisotropic tissue conductivity on electric field distribution in deep brain stimulation. Med. Biol. Eng. Comput. 50, 23–32.
Astrom, M., Diczfalusy, E., Martens, H., Wardell, K., 2015. Relationship between neural activation and electric field distribution during deep brain stimulation. IEEE Trans. Biomed. Eng. 62, 664–672.
Avecillas-Chasin, J.M., Alonso-Frech, F., Nombela, C., Villanueva, C., Barcia, J.A., 2019. Stimulation of the tractography-defined subthalamic nucleus regions correlates with clinical outcomes. Neurosurgery.
Bedard, C., Kroger, H., Destexhe, A., 2004. Modeling extracellular field potentials and the frequency-filtering properties of extracellular space. Biophys. J. 86, 1829–1842.
Benabid, A.L., Chabardes, S., Mitrofanis, J., Pollak, P., 2009. Deep brain stimulation of the subthalamic nucleus for the treatment of Parkinson's disease. Lancet Neurol. 8, 67–81.
Bentley, J.N., Guan, Z., Cummings, K.S., Chou, K.L., Patil, P.G., 2017. Influence of intracranial air on electrode position and clinical outcomes following deep brain stimulation for Parkinson's disease. Stereotact. Funct. Neurosurg. 95, 6–12.
Blomstedt, P., Fytagoridis, A., Astrom, M., Linder, J., Forsgren, L., Hariz, M.I., 2012. Unilateral caudal zona incerta deep brain stimulation for Parkinsonian tremor. Parkinsonism Relat. Disord. 18, 1062–1066.
Bot, M., Schuurman, P.R., Odekerken, V.J.J., Verhagen, R., Contarino, F.M., De Bie, R.M. A., van den Munckhof, P., 2018. Deep brain stimulation for Parkinson's disease: defining the optimal location within the subthalamic nucleus. J. Neurol. Neurosurg. Psychiatry 89, 493–498.
Butson, C.R., 2012. Computational models of neuromodulation. Int. Rev. Neurobiol. 107, 5–22.
Butson, C.R., McIntyre, C.C., 2005. Tissue and electrode capacitance reduce neural activation volumes during deep brain stimulation. Clin. Neurophysiol. 116, 2490–2500.
Butson, C.R., McIntyre, C.C., 2006. Role of electrode design on the volume of tissue activated during deep brain stimulation. J. Neural Eng. 3, 1–8.
Butson, C.R., Cooper, S.E., Henderson, J.M., Wolgamuth, B., McIntyre, C.C., 2011. Probabilistic analysis of activation volumes generated during deep brain stimulation. Neuroimage 54, 2096–2104.
Butson, C.R., Cooper, S.E., Henderson, J.M., McIntyre, C.C., 2006. Predicting the effects of deep brain stimulation with diffusion tensor based electric field models. Med. Image Comput. Comput. Assist. Interv. 9, 429–437.
Butson, C.R., Cooper, S.E., Henderson, J.M., McIntyre, C.C., 2007. Patient-specific analysis of the volume of tissue activated during deep brain stimulation. NeuroImage 34, 661–670.
Caire, F., Ranoux, D., Guehl, D., Burbaud, P., neurochirurgica, C.-E., 2013. A systematic review of studies on anatomical position of electrode contacts used for chronic subthalamic stimulation in Parkinson's disease. Acta Neurochirurgica.
Cardona, H.D.V., Orozco, Á., on, Á.-M.A., 2016. Analysis of the Geometry and Electric Properties of Brain Tissue in Simulation Models for Deep Brain Stimulation. Iberoamerican Congress on ….
Chaturvedi, A., Butson, C.R., Cooper, S.E., McIntyre, C.C., 2006. Subthalamic nucleus deep brain stimulation: accurate axonal threshold prediction with diffusion tensor based electric field models. Conf. Proc. IEEE Eng. Med. Biol. Soc. 1, 1240–1243.

Chaturvedi, A., Butson, C.R., Lempka, S.F., Cooper, S.E., McIntyre, C.C., 2010. Patient-specific models of deep brain stimulation: influence of field model complexity on neural activation predictions. Brain Stimul. 3, 65–67.
Chen, Y., Ge, S., Li, Y., Li, N., Wang, J., Wang, X., Li, J., Jing, J., Su, M., Zheng, Z., Luo, T., Qiu, C., Wang, X., 2018. Role of the cortico-subthalamic hyperdirect pathway in deep brain stimulation for the treatment of Parkinson Disease: a diffusion tensor imaging study. World Neurosurg. 114, e1079–e1085.
Chou, K.L., Taylor, J.L., related disorders, P.-P.G., 2013. The MDS− UPDRS tracks motor and non-motor improvement due to subthalamic nucleus deep brain stimulation in Parkinson disease. Parkinsonism & related disorders.
Collins, K.L., Lehmann, E.M., Patil, P.G., 2010. Deep brain stimulation for movement disorders. Neurobiol. Dis. 38, 338–345.
Conrad, E.C., Mossner, J.M., Chou, K.L., Patil, P.G., 2018. Atlas-independent, electrophysiological mapping of the optimal locus of subthalamic deep brain stimulation for the motor symptoms of Parkinson disease. Stereotact. Funct. Neurosurg. 96, 91–99.
Cubo, R., Fahlstrom, M., Jiltsova, E., Andersson, H., Medvedev, A., 2017. Semi-individualized electrical models in Deep Brain Stimulation: a variability analysis. 2017 Ieee Conference on Control Technology and Applications (Ccta 2017), 517-522.
Cubo, R., Medvedev, A., Test, Å.-M., 2015. Model-based optimization of individualized deep brain stimulation therapy. IEEE Des. Test.
Daniluk, S., K, G.D., Ellias, S.A., Novak, P., Nazzaro, J.M., 2010. Assessment of the variability in the anatomical position and size of the subthalamic nucleus among patients with advanced Parkinson's disease using magnetic resonance imaging. Acta Neurochir (Wien) 152, 201-210; discussion 210.
Deniau, J.M., Degos, B., Bosch, C., Maurice, N., 2010. Deep brain stimulation mechanisms: beyond the concept of local functional inhibition. Eur. J. Neurosci. 32, 1080–1091.
Deuschl, G., Schade-Brittinger, C., Krack, P., Volkmann, J., Schafer, H., Botzel, K., Daniels, C., Deutschlander, A., Dillmann, U., Eisner, W., Gruber, D., Hamel, W., Herzog, J., Hilker, R., Klebe, S., Kloss, M., Koy, J., Krause, M., Kupsch, A., Lorenz, D., Lorenzl, S., Mehdorn, H.M., Moringlane, J.R., Oertel, W., Pinsker, M.O., Reichmann, H., Reuss, A., Schneider, G.H., Schnitzler, A., Steude, U., Sturm, V., Timmermann, L., Tronnier, V., Trottenberg, T., Wojtecki, L., Wolf, E., Poewe, W., Voges, J., German Parkinson Study Group, N.S., 2006. A randomized trial of deep-brain stimulation for Parkinson's disease. New Engl. J. Med. 355, 896–908.
Dickie, D.A., Shenkin, S.D., Anblagan, D., Lee, J., Blesa Cabez, M., Rodriguez, D., Boardman, J.P., Waldman, A., Job, D.E., Wardlaw, J.M., 2017. Whole brain magnetic resonance image atlases: a systematic review of existing atlases and caveats for use in population imaging. Front Neuroinform 11, 1.
Duchin, Y., Shamir, R.R., Patriat, R., Kim, J., Vitek, J.L., Sapiro, G., Harel, N., 2018. Patient-specific anatomical model for deep brain stimulation based on 7 Tesla MRI. PLoS One 13, e0201469.
Falconer, R.A., Rogers, S.L., Shenai, M., 2018. Using directional deep brain stimulation to co-activate the subthalamic nucleus and zona incerta for overlapping essential tremor/parkinson's disease symptoms. Front. Neurol. 9, 544.
Florence, G., Sameshima, K., Fonoff, E.T., Hamani, C., 2016. Deep brain stimulation: more complex than the inhibition of cells and excitation of fibers. Neuroscientist 22, 332–345.
Frankemolle, A.M., Wu, J., Noecker, A.M., Voelcker-Rehage, C., Ho, J.C., Vitek, J.L., McIntyre, C.C., Alberts, J.L., 2010. Reversing cognitive-motor impairments in Parkinson's disease patients using a computational modelling approach to deep brain stimulation programming. Brain 133, 746–761.
Garcia-Gomar, M.G., Soto-Abraham, J., Velasco-Campos, F., Concha, L., 2017. Anatomic characterization of prelemniscal radiations by probabilistic tractography: implications in Parkinson's disease. Brain Struct. Funct. 222, 71–81.
Grant, P.F., Lowery, M.M., 2010. Effect of dispersive conductivity and permittivity in volume conductor models of deep brain stimulation. IEEE Trans. Biomed. Eng. 57, 2386–2393.
Gunalan, K., Chaturvedi, A., Howell, B., Duchin, Y., Lempka, S.F., Patriat, R., Sapiro, G., Harel, N., McIntyre, C.C., 2017. Creating and parameterizing patient-specific deep brain stimulation pathway-activation models using the hyperdirect pathway as an example. PLoS One 12, e0176132.
Gunalan, K., Howell, B., McIntyre, C.C., 2018. Quantifying axonal responses in patient-specific models of subthalamic deep brain stimulation. Neuroimage 172, 263–277.
Guo, S., Zhuang, P., Hallett, M., Zheng, Z., Zhang, Y., Li, J., Li, Y., 2013. Subthalamic deep brain stimulation for Parkinson's disease: correlation between locations of oscillatory activity and optimal site of stimulation. Parkinsonism Relat. Disord. 19, 109–114.
Haegelen, C., Baumgarten, C., Houvenaghel, J.F., Zhao, Y., Peron, J., Drapier, S., Jannin, P., Morandi, X., 2018. Functional atlases for analysis of motor and neuropsychological outcomes after medial globus pallidus and subthalamic stimulation. PLoS One 13, e0200262.
Herzog, J., Fietzek, U., Hamel, W., Morsnowski, A., Steigerwald, F., Schrader, B., Weinert, D., Pfister, G., Muller, D., Mehdorn, H.M., Deuschl, G., Volkmann, J., 2004. Most effective stimulation site in subthalamic deep brain stimulation for Parkinson's disease. Movement Disorders 19, 1050–1054.
Houshmand, L., Cummings, K.S., Chou, K.L., Patil, P.G., 2014. Evaluating indirect subthalamic nucleus targeting with validated 3-tesla magnetic resonance imaging. Stereotact. Funct. Neurosurg. 92, 337–345.
Houshmand, L., 2015. Optimized Targeting in Deep Brain Stimulation for Movement Disorders. Optimized Targeting in Deep Brain Stimulation for Movement Disorders.
Howell, B., McIntyre, C.C., 2016. Analyzing the tradeoff between electrical complexity and accuracy in patient-specific computational models of deep brain stimulation. J. Neural Eng. 13, 036023.
Howell, B., McIntyre, C.C., 2017. Role of soft-tissue heterogeneity in computational models of deep brain stimulation. Brain Stimul. 10, 46–50.
Howell, B., Huynh, B., Grill, W.M., 2015. Design and in vivo evaluation of more efficient and selective deep brain stimulation electrodes. J. Neural Eng. 12, 046030.
Howell, B., Gunalan, K., McIntyre, C.C., 2019. A driving-force predictor for estimating pathway activation in patient-specific models of deep brain stimulation. Neuromodulation 22, 403–415.
Ineichen, C., Shepherd, N.R., Surucu, O., 2018. Understanding the effects and adverse reactions of deep brain stimulation: is it time for a paradigm shift toward a focus on heterogenous biophysical tissue properties instead of electrode design only? Front. Hum. Neurosci. 12, 468.
Jaermann, T., Crelier, G., An …, P.-K.P., 2004. SENSE-DTI at 3 T. … in Medicine: An ….
Johnson, M.D., Miocinovic, S., McIntyre, C.C., Vitek, J.L., 2008. Mechanisms and targets of deep brain stimulation in movement disorders. Neurotherapeutics 5, 294–308.
Kent, A.R., Grill, W.M., 2014. Analysis of deep brain stimulation electrode characteristics for neural recording. J. Neural Eng. 11, 046010.
Kleiner-Fisman, G., Herzog, J., Fisman, D.N., Tamma, F., Lyons, K.E., Pahwa, R., Lang, A. E., Deuschl, G., 2006. Subthalamic nucleus deep brain stimulation: summary and meta-analysis of outcomes. Movement Disorders 21 (Suppl 14), S290–S304.
Koivu, M., Huotarinen, A., Scheperjans, F., Laakso, A., Kivisaari, R., Pekkonen, E., 2018. Motor outcome and electrode location in deep brain stimulation in Parkinson's disease. Brain Behav. 8, e01003.
Lanotte, M.M., Rizzone, M., Bergamasco, B., Faccani, G., Melcarne, A., Lopiano, L., 2002. Deep brain stimulation of the subthalamic nucleus: anatomical, neurophysiological, and outcome correlations with the effects of stimulation. J. Neurol. Neurosurg. Psychiatry 72, 53–58.
Lempka, S.F., McIntyre, C.C., 2013. Theoretical analysis of the local field potential in deep brain stimulation applications. PLoS One 8, e59839.
Logothetis, N.K., Kayser, C., Oeltermann, A., 2007. In vivo measurement of cortical impedance spectrum in monkeys: implications for signal propagation. Neuron 55, 809–823.
Lu, C.W., Chou, K.L., Patil, P.G., 2020a. Correspondence of optimal stimulation and beta power varies regionally in STN DBS for Parkinson disease. Parkinsonism Relat. Disord. 78, 124–128.
Lu, C.W., Malaga, K.A., Chou, K.L., Chestek, C.A., Patil, P.G., 2020b. High density microelectrode recording predicts span of therapeutic tissue activation volumes in subthalamic deep brain stimulation for Parkinson disease. Brain Stimul. 13, 412–419.
Madler, B., Coenen, V.A., 2012. Explaining clinical effects of deep brain stimulation through simplified target-specific modeling of the volume of activated tissue. AJNR Am. J. Neuroradiol. 33, 1072–1080.
Maks, C.B., Butson, C.R., Walter, B.L., Vitek, J.L., McIntyre, C.C., 2009. Deep brain stimulation activation volumes and their association with neurophysiological mapping and therapeutic outcomes. J. Neurol. Neurosurg. Psychiatry 80, 659–666.
Massey, L.A., Miranda, M.A., Zrinzo, L., Al-Helli, O., Parkes, H.G., Thornton, J.S., So, P. W., White, M.J., Mancini, L., Strand, C., Holton, J.L., Hariz, M.I., Lees, A.J., Revesz, T., Yousry, T.A., 2012. High resolution MR anatomy of the subthalamic nucleus: imaging at 9.4 T with histological validation. NeuroImage 59, 2035–2044.
McClelland 3rd, S., Ford, B., Senatus, P.B., Winfield, L.M., Du, Y.E., Pullman, S.L., Yu, Q., Frucht, S.J., McKhann 2nd, G.M., Goodman, R.R., 2005. Subthalamic stimulation for Parkinson disease: determination of electrode location necessary for clinical efficacy. Neurosurg. Focus 19, E12.
McIntyre, C.C., Grill, W.M., Sherman, D.L., Thakor, N.V., 2004a. Cellular effects of deep brain stimulation: model-based analysis of activation and inhibition. J. Neurophysiol. 91, 1457–1469.
McIntyre, C.C., Mori, S., Sherman, D.L., Thakor, N.V., Vitek, J.L., 2004b. Electric field and stimulating influence generated by deep brain stimulation of the subthalamic nucleus. Clin. Neurophysiol. 115, 589–595.
McIntyre, C.C., Savasta, M., Kerkerian-Le Goff, L., Vitek, J.L., 2004c. Uncovering the mechanism(s) of action of deep brain stimulation: activation, inhibition, or both. Clin. Neurophysiol. 115, 1239–1248.
McIntyre, C.C., Frankenmolle, A.M., Wu, J., Noecker, A.M., Alberts, J.L., 2009. Customizing deep brain stimulation to the patient using computational models. In: Conf Proc IEEE Eng Med Biol Soc 2009, pp. 4228–4229.
McIntyre, C.C., Hahn, P.J., 2010. Network perspectives on the mechanisms of deep brain stimulation. Neurobiol. Dis. 38, 329–337.
Miocinovic, S., Parent, M., Butson, C.R., Hahn, P.J., Russo, G.S., Vitek, J.L., McIntyre, C. C., 2006. Computational analysis of subthalamic nucleus and lenticular fasciculus activation during therapeutic deep brain stimulation. J. Neurophysiol. 96, 1569–1580.
Miocinovic, S., Lempka, S.F., Russo, G.S., Maks, C.B., Butson, C.R., Sakaie, K.E., Vitek, J. L., McIntyre, C.C., 2009. Experimental and theoretical characterization of the voltage distribution generated by deep brain stimulation. Exp. Neurol. 216, 166–176.
Montgomery Jr., E.B., Gale, J.T., 2008. Mechanisms of action of deep brain stimulation (DBS). Neurosci. Biobehav. Rev. 32, 388–407.
Nestor, K.A., Jones, J.D., Butson, C.R., Morishita, T., Jacobson, C.E.t., Peace, D.A., Chen, D., Foote, K.D., Okun, M.S., 2014. Coordinate-based lead location does not predict Parkinson's disease deep brain stimulation outcome. PLoS One 9, e93524.
Nowacki, A., Nguyen, T.A., Tinkhauser, G., Petermann, K., Debove, I., Wiest, R., Pollo, C., 2018. Accuracy of different three-dimensional subcortical human brain atlases for DBS -lead localisation. Neuroimage Clin. 20, 868–874.
O'Halloran, R.L., Chartrain, A.G., neurosurgery, R.-J.J., 2016. Case Study of Image-Guided Deep Brain Stimulation: Magnetic Resonance Imaging–Based White Matter Tractography Shows Differences in Responders and …. World neurosurgery.

Okun, M.S., 2012. Deep-brain stimulation for Parkinson's disease. New Engl. J. Med. 367, 1529–1538.
Okun, M.S., Tagliati, M., Pourfar, M., Fernandez, H.H., Rodriguez, R.L., Alterman, R.L., Foote, K.D., 2005. Management of referred deep brain stimulation failures: a retrospective analysis from 2 movement disorders centers. Arch. Neurol. 62, 1250–1255.
Paek, S.H., Han, J.H., Lee, J.Y., Kim, C., Jeon, B.S., Kim, D.G., 2008. Electrode position determined by fused images of preoperative and postoperative magnetic resonance imaging and surgical outcome after subthalamic nucleus deep brain stimulation. Neurosurgery 63, 925-936; discussion 936-927.
Patel, N., Khan, S., Gill, S., 2008. Comparison of atlas-and magnetic-resonance-imaging-based stereotactic targeting of the subthalamic nucleus in the surgical treatment of Parkinsonís disease. Stereotact. Funct. Neurosurg. 86, 153–161.
Patil, P.G., Conrad, E.C., Aldridge, J.W., Chenevert, T.L., Chou, K.L., 2012. The anatomical and electrophysiological subthalamic nucleus visualized by 3-T magnetic resonance imaging. Neurosurgery 71, 1089–1095 discussion 1095.
Pelot, N.A., Thio, B.J., Grill, W.M., 2018. Modeling current sources for neural stimulation in COMSOL. Front. Comput. Neurosci. 12, 40.
Plaha, P., Ben-Shlomo, Y., Patel, N.K., Gill, S.S., 2006. Stimulation of the caudal zona incerta is superior to stimulation of the subthalamic nucleus in improving contralateral parkinsonism. Brain 129, 1732–1747.
Pollo, C., Vingerhoets, F., Pralong, E., Ghika, J., Maeder, P., Meuli, R., Thiran, J.P., Villemure, J.G., 2007. Localization of electrodes in the subthalamic nucleus on magnetic resonance imaging. J. Neurosurg. 106, 36–44.
Richardson, R.M., Ostrem, J.L., Starr, P.A., 2009. Surgical repositioning of misplaced subthalamic electrodes in Parkinson's disease: location of effective and ineffective leads. Stereotact. Funct. Neurosurg. 87, 297–303.
Richter, E.O., Hoque, T., Halliday, W., Lozano, A.M., Saint-Cyr, J.A., 2004. Determining the position and size of the subthalamic nucleus based on magnetic resonance imaging results in patients with advanced Parkinson disease. J. Neurosurg. 100, 541–546.
Rodrigues, N.B., Mithani, K., Meng, Y., Lipsman, N., Hamani, C., 2018. The emerging role of tractography in deep brain stimulation: basic principles and current applications. Brain Sci. 8, 23.
Schmidt, C., Grant, P., Lowery, M., van Rienen, U., 2013. Influence of uncertainties in the material properties of brain tissue on the probabilistic volume of tissue activated. IEEE Trans. Biomed. Eng. 60, 1378–1387.
Schmidt, C., van Rienen, U., 2012. Modeling the field distribution in deep brain stimulation: the influence of anisotropy of brain tissue. IEEE Trans. Biomed. Eng. 59, 1583–1592.
Studholme, C., Hawkes, D.J., Hill, D.L.G., 1998. Normalized entropy measure for multimodality image alignment. Medical Imaging 1998: Image Processing.
Talairach, J., Tournoux, P., 1988. Co-planar stereotaxic atlas of the human brain. 3-Dimensional proportional system: an approach to cerebral imaging. Co-planar stereotaxic atlas of the human brain. 3-Dimensional proportional system: an approach to cerebral imaging.
Telkes, I., Viswanathan, A., Jimenez-Shahed, J., Abosch, A., Ozturk, M., Gupte, A., Jankovic, J., Ince, N.F., 2018. Local field potentials of subthalamic nucleus contain electrophysiological footprints of motor subtypes of Parkinson's disease. Proc. Natl. Acad. Sci. U.S.A. 115, E8567–E8576.
Tuch, D.S., Wedeen, V.J., Dale, A.M., George, J.S., Belliveau, J.W., 2001. Conductivity tensor mapping of the human brain using diffusion tensor MRI. Proc. Natl. Acad. Sci. U.S.A. 98, 11697–11701.
van Dijk, K.J., Verhagen, R., Chaturvedi, A., McIntyre, C.C., Bour, L.J., Heida, C., Veltink, P.H., 2015. A novel lead design enables selective deep brain stimulation of neural populations in the subthalamic region. J. Neural Eng. 12, 046003.
van Wijk, B.C.M., Pogosyan, A., Hariz, M.I., Akram, H., Foltynie, T., Limousin, P., Horn, A., Ewert, S., Brown, P., Litvak, V., 2017. Localization of beta and high-frequency oscillations within the subthalamic nucleus region. Neuroimage Clin. 16, 175–183.
Verhagen, R., Bour, L.J., Odekerken, V.J.J., van den Munckhof, P., Schuurman, P.R., de Bie, R.M.A., 2019. Electrode location in a microelectrode recording-based model of the subthalamic nucleus can predict motor improvement after deep brain stimulation for parkinson's disease. Brain Sci. 9.
Vitek, J.L., 2002. Mechanisms of deep brain stimulation: excitation or inhibition. Movement Disorders 17 (Suppl 3), S69–S72.
Voges, J., Volkmann, J., Allert, N., Lehrke, R., Koulousakis, A., Freund, H.J., Sturm, V., 2002. Bilateral high-frequency stimulation in the subthalamic nucleus for the treatment of Parkinson disease: correlation of therapeutic effect with anatomical electrode position. J. Neurosurg. 96, 269–279.
Welter, M.L., Schupbach, M., Czernecki, V., Karachi, C., Fernandez-Vidal, S., Golmard, J. L., Serra, G., Navarro, S., Welaratne, A., Hartmann, A., Mesnage, V., Pineau, F., Cornu, P., Pidoux, B., Worbe, Y., Zikos, P., Grabli, D., Galanaud, D., Bonnet, A.M., Belaid, H., Dormont, D., Vidailhet, M., Mallet, L., Houeto, J.L., Bardinet, E., Yelnik, J., Agid, Y., 2014. Optimal target localization for subthalamic stimulation in patients with Parkinson disease. Neurology 82, 1352–1361.
Wodarg, F., Herzog, J., Reese, R., Movement …, F.-D., 2012. Stimulation site within the MRI-defined STN predicts postoperative motor outcome. Movement ….
Xiao, Y., Jannin, P., D'Albis, T., Guizard, N., Haegelen, C., Lalys, F., Verin, M., Collins, D. L., 2014. Investigation of morphometric variability of subthalamic nucleus, red nucleus, and substantia nigra in advanced Parkinson's disease patients using automatic segmentation and PCA-based analysis. Hum. Brain Mapp. 35, 4330–4344.
Yokoyama, T., Ando, N., Sugiyama, K., Akamine, S., Namba, H., 2006. Relationship of stimulation site location within the subthalamic nucleus region to clinical effects on parkinsonian symptoms. Stereotact. Funct. Neurosurg. 84, 170–175.
Zitella, L.M., Mohsenian, K., Pahwa, M., Gloeckner, C., Johnson, M.D., 2013. Computational modeling of pedunculopontine nucleus deep brain stimulation. J. Neural Eng. 10, 045005.
Zitella, L.M., Teplitzky, B.A., Yager, P., Hudson, H.M., Brintz, K., Duchin, Y., Harel, N., Vitek, J.L., Baker, K.B., Johnson, M.D., 2015. Subject-specific computational modeling of DBS in the PPTg area. Front. Comput. Neurosci. 9, 93.